On the application of the Kitagawa–Takahashi diagram to foreign-object damage and high-cycle fatigue

J.O. Peters [a,1], B.L. Boyce [a,2], X. Chen [b], J.M. McNaney [a], J.W. Hutchinson [b], R.O. Ritchie [a,*]

[a] *Department of Materials Science and Engineering, University of California, Berkeley, CA 94720-1760, USA*
[b] *Division of Applied Sciences, Harvard University, Cambridge, MA 02138, USA*

Abstract

The role of foreign-object damage (FOD) and its effect on high-cycle fatigue (HGF) failures in a turbine engine Ti–6Al–4V alloy is examined in the context of the use of the Kitagawa–Takahashi diagram to describe the limiting conditions for such failures. Experimentally, FOD is simulated by firing 1 and 3.2 mm diameter steel spheres onto the flat specimen surface of tensile fatigue specimens at velocities of 200 and 300 m/s. Such damage was found to markedly reduce the fatigue strength of the alloy, primarily due to four factors: stress concentration, microcrack formation, impact-induced plasticity and tensile residual stresses associated with the impact damage. Two groups of fatigue failures could be identified. The first group initiated directly at the impact site, and can be readily described through the use of a fatigue-crack growth threshold concept. Specifically, a Kitagawa–Takahashi approach is presented where the limiting threshold conditions are defined by the stress-concentration corrected smooth-bar fatigue limit (at microstructurally small crack sizes) and a ''worst-case'' fatigue-crack growth threshold (at larger crack sizes). The second group of failures was caused by fatigue cracks that initiated at locations far from the impact site in regions of high tensile residual stresses, the magnitude of which was computed numerically and measured experimentally using synchrotron X-ray diffraction. Specifically, these failures could be rationalized due to the superposition of the residual stresses on the far-field applied mean stress, leading to a locally elevated load ratio (ratio of minimum to maximum loads). The effects of residual stress, stress concentration, and microstructurally small cracks are combined in a modified Kitagawa–Takahashi approach to provide a mechanistic basis for evaluating the detrimental effect of FOD on HCF failures in Ti–6Al–4V blade alloys. © 2002 Elsevier Science Ltd. All rights reserved.

Keywords: Ti–6Al–4V; Foreign-object damage; High-cycle fatigue; Residual stress; Fatigue-crack initiation; Fatigue-crack growth threshold

---

[*] Corresponding author. Tel.: +1-510-486-5798; fax: +1-510-486-4881.
E-mail address: roritchie@lbl.gov (R.O. Ritchie).
[1] Now with Department of Physical Metallurgy and Materials Technology, Technical University Hamburg-Harburg, 21071 Hamburg, Germany.
[2] Now with Sandia National Laboratories, P.O. Box 5800, MS 0899, Albuquerque, NM 87185-0899, USA.

1. Introduction

High-cycle fatigue (HCF) of turbine engine disk and blade components represents one of the major concerns limiting the readiness and safety of military aircraft. Since *in-flight* HCF conditions invariably involve high cyclic frequencies, small crack sizes and (in some airfoil locations) very high mean stress levels, a preferred fracture-mechanics based approach for design against HCF can be based on the concept of a limiting threshold for no fatigue-crack growth [1–7]. Foreign-object damage (FOD) by hard particles, such as stones ingested into the compressor, has been identified as one of the key factors associated with such HCF related failures in titanium alloy blades [1–4]. Specifically, FOD has been found to reduce the fatigue strength of fan and compressor blades, principally by causing stress-raising notches [5,6] and microcracks [6] at impact sites; this, in association with the plastic deformation [4] and tensile residual stresses [4] resulting from such impacts, can lead to the early nucleation and growth of fatigue cracks.

Recent studies [8–10] on the HCF properties of an $\alpha + \beta$ processed Ti–6Al–4V blade alloy, where FOD was simulated using high-velocity impacts of steel shot on a flat surface, have focused primarily on the definition of threshold conditions for crack initiation and growth during subsequent fatigue cycling. The mechanistic effect of FOD was considered in terms of (i) the possibility of microcrack formation in the damage zone, (ii) the stress concentration associated with the shape of the impact crater, (iii) microstructural damage from FOD-induced plastic deformation, and (iv) the presence of localized tensile residual hoop stresses in the vicinity of the impact site. Although all of these factors play an important role under certain conditions, in the case of high impact velocities (300 m/s) the formation of damage-induced microcracks appears to be the primary contributor to lifetime reduction. During subsequent cycling after impact, these microcracks, which are formed in the pile-up of material around the rim, can act as preferred sites for propagating fatigue cracks. When applied stresses are large compared to the impact-induced tensile residual stresses, and in the presence of relatively large ($\sim$30–50 μm) impact-induced microcracks, HCF failures (within 10^5–10^6 cycles) initiate directly *at* the impact site and lead to short fatigue lives. In contrast, at low-applied stresses relative to the residual stresses, HCF failures (after 10^7–10^8 cycles) initiate in locations *away* from the impact site at regions of peak tensile residual stress, and the necessity for crack nucleation leads to longer fatigue lives.

In analyzing the high stress failures, it was found that FOD-initiated microcracks, together with the stress concentration of the indent, were the prime reasons that the HCF failures initiated at the FOD sites. The microcracks (some as small as 1 μm) grew at applied stress intensities as low as $\Delta K = 1$ MPa $\sqrt{m}$, which is well below the ''worst-case'' ΔK_{TH} threshold in this material [11] of 1.9 MPa $\sqrt{m}$ based on the propagation of large cracks (macroscopic ''homogeneous continuum-sized'' cracks which are considerably larger than the scale of the microstructure). This worst-case threshold had previously been defined at elevated mean loads (or load ratios, i.e., the ratio of minimum to maximum loads, in excess of $R = 0.9$) in an attempt to eliminate effects of crack closure and to provide a lower-bound threshold for propagation [11]. However, it is clear that this threshold is only relevant to cracks larger than the scale of the microstructure, i.e., $\sim$50–100 μm length in the current microstructure. Since the microcracks associated with impact damage are more than an order-of-magnitude smaller than this, an alternative approach was proposed [9,10] to describe the threshold HCF conditions in the presence of FOD. This approach was based on a Kitagawa–Takahashi diagram where the limiting conditions for failure in this case were defined in terms of the stress-concentration corrected smooth-bar fatigue limit (at microstructurally small cracks sizes) and the ''worst-case'' threshold (at larger, ''homogeneous continuum-sized'' crack sizes).

In contrast to HCF failures under such high-applied stresses, at low-applied stress ranges failures were caused by fatigue cracks that initiated at locations far from the impact site, specifically in regions of high tensile residual stresses. Accordingly, it is the primary purpose of this study to further examine the utility of the Kitagawa–Takahashi approach to provide a general description of HCF failures in impact damaged Ti–6Al–4V. Specifically, we investigate the role of the relative magnitudes of the applied and residual stresses in

dictating the sites for the initiation of HCF failures, in order to provide a methodology to describe the limiting threshold conditions for such failures at both low- and high-applied cyclic stresses. To achieve this objective, the magnitudes of the residual stresses in the vicinity of various damage sites are computed numerically [12] and measured experimentally using spatially resolved synchrotron X-ray diffraction (with spot sizes on the order of 300×300 μm^2) [13]. Such stresses are thought to alter the local mean stress (or load ratio) for subsequent fatigue cracking. The role of load ratio on fatigue life is evaluated by determining smooth-bar stress-life (S–N) curves over a wide range of load ratios from $R = -1$ to 0.8. Using such results, a modified Kitagawa–Takahashi approach is presented to provide a phenomenological understanding of the effect of FOD on HCF failures in Ti–6Al–4V.

2. Experimental procedures

2.1. Material

The Ti–6Al–4V alloy under investigation was part of a set of forgings produced specifically for the U.S. Air Force sponsored National High-Cycle Fatigue Program, and is representative of material typically used in the front compressor stages of the turbine engine. The chemical composition is given in Table 1. The bimodal microstructure of the plate material, consisting of ∼60% primary α (grain size ∼ 20 μm) within a lamellar α + β matrix, is shown in Fig. 1; this condition has also been termed "solution treated and overaged" (STOA). Material and processing details are given in Refs. [8,14]. Uniaxial tensile properties, based on tests parallel to the length of the plate, are listed in Table 2.

Table 1
Chemical composition of Ti–6Al–4V bar stock material in wt.% [14]

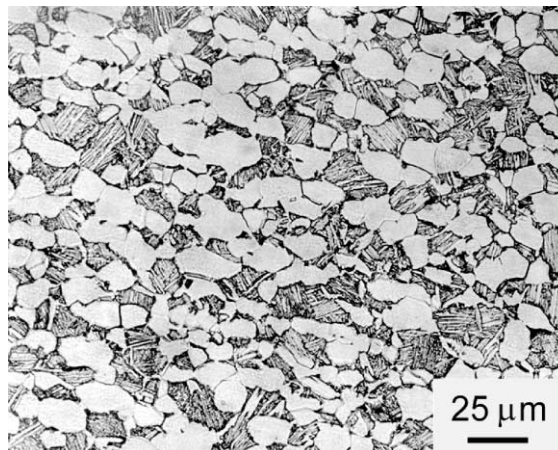| Ti	Al	V	Fe	O	N	H
Bal.	6.30	4.19	0.19	0.19	0.013	0.0041

Fig. 1. Optical micrograph of the bimodal (STOA) microstructure of forged Ti–6Al–4V plate material.

Table 2
Uniaxial tensile properties of bimodal Ti–6Al–4V

E (GPa)	$\sigma_{0.2}$ (MPa)	UTS (MPa)	σ_f (MPa)	Elong. (%)	RA (%)
110	915	965	1310	19	45

E: Young's modulus, $\sigma_{0.2}$: yield stress, UTS: ultimate tensile strength, σ_f: true fracture stress, Elong.: tensile elongation, RA: reduction of area at fracture; strain rate 8×10^{-4} s^{-1}.

2.2. Simulation of foreign-object damage

FOD was simulated by firing 1 or 3.2 mm diameter chrome-hardened steel spheres onto a flat specimen surface of tensile fatigue (so-called ''K_B'') specimens at angles of 60° and 90° (see Fig. 2), and at velocities of 200 and 300 m/s using a compressed-gas gun facility. Such impact velocities represent typical in-service impact velocities on aircraft engine fan blades, with the 300 m/s velocities representing a worst-case. The impact damage craters are also of a size typical of those seen in service, with root radii similar to those of actual damage sites [6].

2.3. Fatigue test methods

To evaluate the smooth-bar fatigue limit of the bimodal Ti–6Al–4V alloy, previous *S–N* data [15] have been complemented by 25 Hz tests (for shorter lives $<10^6$ cycles) and 1000 Hz tests (for longer lives $>10^6$ cycles) on hourglass specimens with minimum diameters of 3.0 mm (25 Hz) and 5.4 mm (1000 Hz). (No effect of frequency on near-threshold fatigue-crack propagation is apparent in this alloy between 50 and 20,000 Hz for tests in ambient air environments [11].) Specifically, 1000 Hz tests were conducted on an automated MTS servo-hydraulic testing machine, with a newly developed system using a voice-coil ser-vovalve (further details are described in Ref. [16]). To obtain a nominally stress-free surface, specimens were stress relieved in vacuo for 2 h at 705 °C prior to chemically milling in a solution of 50 ml HF, 500 ml HNO_3 and 1500 ml H_2O. For all tests, the loading direction of the specimen was parallel to the long axis of the forged plate.

K_B specimens were used to study the effect of FOD on the fatigue strength of Ti–6Al–4V. These samples have a rectangular cross-section of 3.2×7.2 mm^2, a gauge length of 20 mm and cylindrical buttonhead ends. As with the hourglass samples, they were prepared with a ''stress-free'' surface (in the gauge length) using stress relief and chemical-milling procedures. After impacting with the steel spheres to simulate FOD, the damaged regions were examined for the presence of potential crack initiation sites or microcracks in a
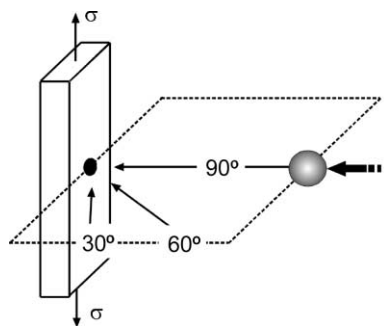

Fig. 2. Schematic illustration showing impact angles with respect to specimen geometry and loading axis for fatigue tests. In this study, normal (90°) and inclined (60°) impact angles were chosen.

high-resolution LEO 1550 field-emission scanning electron microscope (SEM), prior to cycling at maximum stress values between 225 and 500 MPa at $R = 0.1$ and 0.5 (with a sinusoidal waveform). Throughout fatigue testing, specimens were periodically removed from the test frame and the progress of crack initiation and growth at the surface of the impact site was examined in the SEM. The position of the crack front during crack extension, both on the surface and depthwise, was determined from two sets of measurements. The surface crack length was measured periodically during the fatigue test in the SEM; the crack depth was estimated by subsequent fractography as the local crack front is oriented perpendicular to the "river markings". For the bimodal Ti–6Al–4V alloy, growing fatigue cracks had an approximate crack depth, a, to surface crack length, $2c$, ratio of $a/2c \sim 0.45$ [8]. After converting the surface crack length into crack depth, the rate of crack extension caused by the fatigue loading was computed using standard finite-difference procedures (with no smoothing routines) and expressed in terms of average crack extension per cycle (da/dN).

To define stress-intensity values for the thresholds and early fatigue-crack growth conditions associated with microcracks at the impact site, the relationship of Lukáš [17] for small cracks at notches was utilized, which includes both indentation geometry and stress-concentration effects:

$$\Delta K = \frac{0.7k_t}{\sqrt{1 + 4.5(a/\rho)}} \Delta\sigma \sqrt{\pi a}. \tag{1}$$

In Eq. (1), k_t is the elastic stress-concentration factor, $\Delta\sigma$ is the stress range, a is the crack depth, and ρ is the indentation radius. The factor of 0.7 is based on the stress-intensity boundary correction and the crack-shape correction factors for semi-elliptical surface cracks ($a/2c \sim 0.45$) [18].

Table 3 lists the impact site dimensions and the resulting elastic stress-concentration factors according to photoelastic experiments [19]. The stress concentration is at a maximum at the base of the impact indentation sites, with values ranging from $k_t = 1.8$ (for 1 mm shot at 300 m/s) to $k_t = 1.4$ (for 3.2 mm shot at 200 m/s). Corresponding values at the crater rim range from $k_t = 1.3$ (1 mm shot, 300 m/s) to $k_t = 1.15$ (3.2 mm shots, 200 m/s). These k_t-values for the crater rim are identical to those computed recently by three-dimensional numerical analysis [12]; however, values for the indent base are $\sim 10\%$ higher. Corresponding elastic stress-concentration factors for inclined impacts are also listed in Table 3.

It should be noted, that there might be some concern over the application of linear-elastic fracture mechanics to such microcracks where crack sizes may be comparable to the scale of the microstructure and crack-tip plasticity. With respect to the scale of microstructure, it is known that misorientations between individual α grains and the high density of grain boundaries in globular or bimodal titanium alloys

Table 3
Ti–6Al–4V, summary of impact conditions, fatigue loading and crack initiation sites

Impact condition	Velocity (m/s)	Crater width (mm)	Crater depth (mm)	k_t (base)	k_t (rim)	σ_{max}, $R = 0.1$ (MPa)	Crack initiation	Cycles at failure
1 mm, 90°	300	0.93	0.26	1.8	1.30	500	Rim	3.2×10^5
1 mm, 90°	300	0.93	0.26	1.8	1.30	325	Interior	1.3×10^8
3.2 mm, 90°	300	2.67	0.67	1.6	1.25	500	Rim	$3–6 \times 10^4$
3.2 mm, 90°	300	2.67	0.67	1.6	1.25	325	Rim, interior, side*	5×10^5–1.7×10^7
3.2 mm, 90°	200	2.14	0.43	1.4	1.15	500	Base	8×10^4–1.4×10^5
3.2 mm, 90°	200	2.14	0.43	1.4	1.15	325	Side*	1.5×10^7
3.2 mm, 60°	300	2.58	0.67	1.6	1.25	500	Rim	5×10^4
3.2 mm, 60°	300	2.58	0.67	1.6	1.25	325	Rim	5×10^5
3.2 mm, 60°	200	1.93	0.34	1.3	1.10	500	Rim	1.2×10^5
3.2 mm, 60°	200	1.93	0.34	1.3	1.10	325	Interior	1.5×10^8

* Side face of K_B sample.

significantly affect *local* driving forces and hence the crack-growth rates of microstructurally small cracks [15,20,21]. However, in case of FOD impacts, the resulting highly plastically deformed microstructure with its inherently high dislocation density [9] effectively tends to lessen this influence of the local orientation of microstructural features. With respect to the corresponding scale of the plastic zone ahead of the crack tip, in the near-threshold regime of $\Delta K \sim 1$–2 MPa $\sqrt{m}$, computed maximum plastic zone sizes are only ~ 0.2–1 μm for 1–10 μm sized cracks, and therefore such conditions are close to those of small-scale yielding. Furthermore, the contribution of the residual stresses is not included in the ΔK calculation in Eq. (1), since to the first approximation these stresses will not change the value of the stress-intensity range. They do, however, affect the mean stress and hence alter the local load ratio, as is specifically addressed in this paper.

3. Results and discussion

3.1. Smooth-bar fatigue: surface vs. subsurface initiation

To investigate the role of impact-induced tensile residual stresses acting as a mean stress superimposed on the applied fatigue stress range, smooth-bar S–N fatigue tests were performed over a wide range of mean stress values, i.e., over a range of load ratios from $R = -1$ to 0.8. Resulting smooth-bar S–N fatigue properties of the bimodal Ti–6Al–4V material are shown in Fig. 3(a) and (b) in terms of the cyclic maxi-
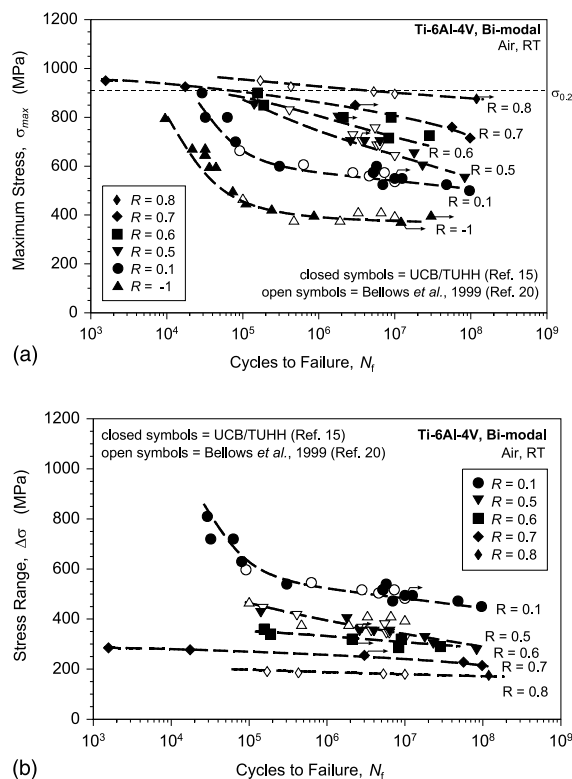

Fig. 3. Stress-life (S–N) curves for bimodal Ti–6Al–4V, determined using smooth-bar specimens at load ratios from $R = -1$ to 0.8 in terms of (a) maximum stress, σ_{max}, and (b) stress range, $\Delta\sigma$. Previously published results from Ref. [15] are complemented by 20 and 1000 Hz data. Also shown are S–N data (open symbols) of the same material published by Bellows et al. [22].
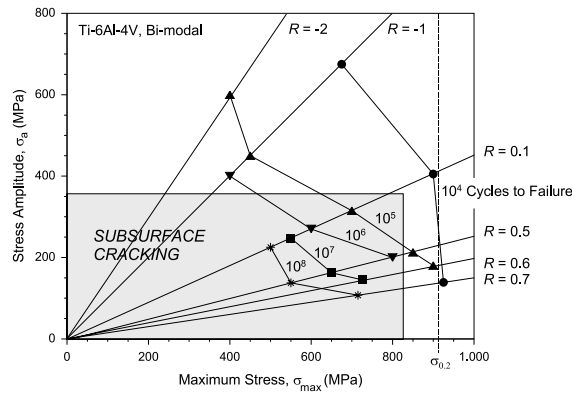
Fig. 4. Subsurface failure envelope for smooth-bar bimodal Ti–6Al–4V specimens, determined at load ratios ranging from $R = -2$ to 0.7. The failure envelope indicates the occurrence of subsurface crack initiation with both decreasing stress amplitude, σ_a, and maximum stress values, σ_{max}.

mum stress and cyclic stress range, together with previously published fatigue results [15,22]. These data indicate that an increase in mean stress, and hence load ratio, leads to an increase in the limiting value of maximum applied stress necessary to cause HCF failure (Fig. 3(a)); however, the corresponding limiting applied stress range $\Delta\sigma$ is markedly decreased (Fig. 3(b)).

Crack initiation sites were examined as a function of the maximum and alternating stresses. Under fully reversed loading ($R = -1$), fatigue cracks were found to initiate at the specimen surface [15], whereas at positive load ratios ($R = 0.1$–0.8), initiation was generally subsurface. The occurrence of subsurface crack initiation in smooth-bar test specimens can be best described in a plot of stress amplitude vs. maximum stress (Fig. 4). The resulting subsurface failure envelope displayed in Fig. 4 clearly shows that interplay of both relatively low stress amplitude and maximum stress level results in subsurface cracking in smooth-bar samples. In addition, it was found that the crack initiation site moved from regions close to the surface ($\sim$40–100 μm) to farther into the interior ($\sim$250–450 μm) with decreasing stress amplitude; this led to a corresponding increase in fatigue life at a given load ratio. Specifically, at fatigue lives greater than $\sim$5 × 10^7 cycles, cracks initiated in regions 250–450 μm below the surface (cf. Fig. 5(a) and (b) for $R = 0.1$). An example of such a high-R ($= 0.7$) fatigue-crack initiation farther in the interior is shown in Fig. 6(a). As reported previously for Ti–6Al–4V [22,23], at even higher maximum applied stresses exceeding the yield stress, fatigue failures occur entirely by ductile rupture, as shown for high-R loading in Fig. 6(b).

Subsurface crack initiation is not common in fatigue, but has become increasingly reported of late for fatigue failures under very long life conditions, particularly in titanium alloys and steels [24–27]. Most traditional explanations for this phenomenon rely on the presence of processing-induced surface compressive residual stresses, i.e., due to heat treatment, case-hardening, or shot-peening procedures. Other explanations include the formation of compressive residual stresses due to preferential plastic deformation at the surface under tension–tension loading [28], or the larger volume of material contained in the interior compared to the surface and hence the higher probability of finding a stress-raising defect (e.g., inclusions in steels) or a weak microstructural orientation (e.g., in titanium alloys). In the present experiments, the as-tested surfaces were nominally stress free (verified by X-ray diffraction), and therefore it is believed that the subsurface initiation is the result of the latter effect. Indeed, Evans and Bache [29] have recently pointed out the significance of such weak microstructural orientations, and the related stress redistribution between individual grains as the cause of premature crack initiation in titanium alloys.
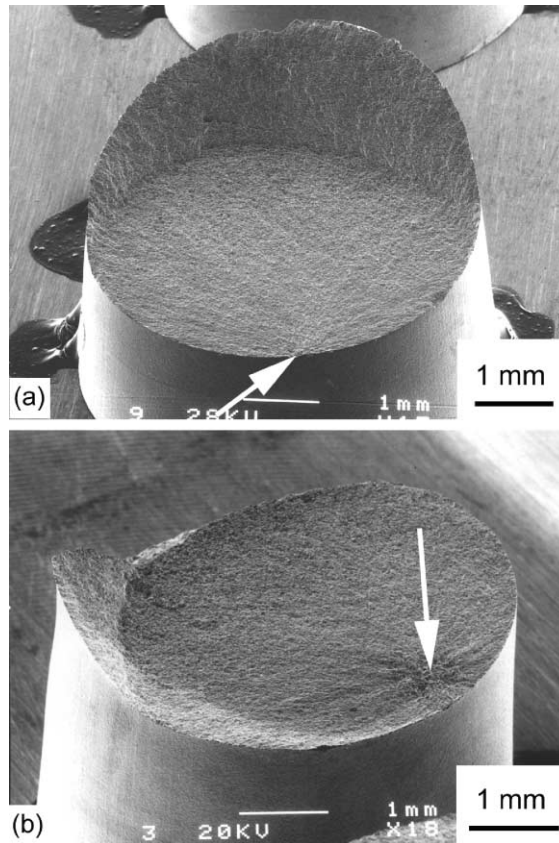
Fig. 5. At low load ratio of $R = 0.1$, fatigue cracks initiated (a) close to the surface ($\sigma_{max} = 525$ MPa, $N_f = 4.8 \times 10^7$ cycles), and (b) in the interior away from the surface ($\sigma_{max} = 500$ MPa, $N_f = 9.6 \times 10^7$ cycles).

A typical subsurface HCF crack initiation site in the bimodal Ti–6Al–4V alloy is shown in Fig. 7(a). Higher magnification imaging (Fig. 7(b)) revealed a facet-type fracture surface, involving crack initiation and early growth along planar slip bands. The facets of fractured α grains, which were aligned perpendicular to stress axis, were of near-basal orientation, based on electron backscattered diffraction (EBSD) analysis.

3.2. Impact-induced damage state

A wide variety of impact conditions was investigated in this study. The flat surface of the rectangular gauge section of K_B specimens was impacted at angles of 90° (normal impact) and 60° (Fig. 2) using impact velocities of 200–300 m/s. Steel shot of 3.2 mm diameter was used for normal and inclined impacts; additionally, 1 mm steel shot was also used for 300 m/s normal impact experiments. All impact conditions and consequent impact geometries used in this study are listed in Table 3. Examples of damage sites on the flat surface of K_B specimens, resulting from 300 m/s normal impacts (90°) with 1 and 3.2 mm steel shot, show similar features. From dimensional analysis, the indentation depth, crater diameter and plastic pile-up scale with the size of the foreign object, and only depend on the impact velocity. Therefore, the resulting geo-
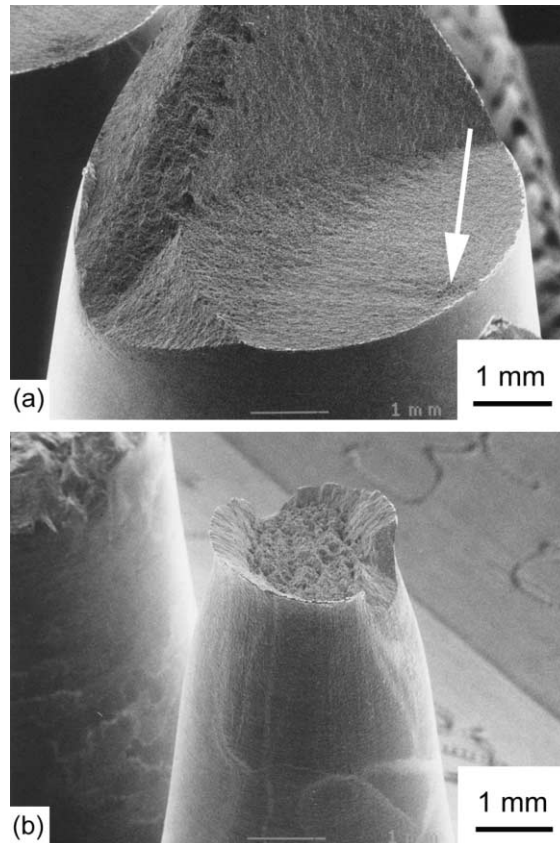
Fig. 6. At a high load ratio of $R = 0.7$ and (a) maximum stress values below yield stress, the fatigue-crack initiation mechanism is the same as low $R = 0.1$ failures ($\sigma_{max} = 725$ MPa, $N_f = 9.8 \times 10^7$ cycles); however, (b) maximum applied stress values exceeding the yield stress resulted in gross plasticity and ductile tensile fracture ($\sigma_{max} = 925$ MPa, $N_f = 1.7 \times 10^4$ cycles).

metric features of the impact craters are virtually the same for 300 m/s normal impacts (90°) with either size of projectile, despite the order-of-magnitude difference in kinetic energy involved [30].

Increasing impact velocity has previously been associated with increasingly severe damage states in the present material [8–10]. For impact velocities in excess of ~250 m/s, pile-up of material at the crater rim (Fig. 8) resulted in the formation of multiple micronotches and microcracks (insert in Fig. 9). Moreover, rings of circumferentially oriented shear bands were formed within the impact crater, emanating from the surface into the material beneath the damaged site. For both the 3.2 and 1 mm diameter steel shot, the microcracks (~2–50 μm in length) formed in 300 m/s impacts provided the nucleation sites for crack growth on subsequent cycling (Fig. 9). Such microcracking was not apparent at slower 200 m/s impacts. *For this reason, we believe that low-velocity or quasi-static indentations do not provide a worst-case simulation of FOD conditions* [8–10].

Scanning electron micrographs and cross-sections of 300 m/s impacts using 3.2 mm steel spheres for 90° and 60° impact angles are shown in Figs. 10 and 11, respectively. Whereas the 90° impact angle resulted in symmetrical impact site, the 60° impact angle created a significantly larger plastic pile-up at the exit side of the crater rim as compared to the entry side. However, the depth of the impact site, the maximum size of pile-up and the associated micronotch/microcrack formation at crater rim were similar for both 60° and 90° impact angles (Table 3).
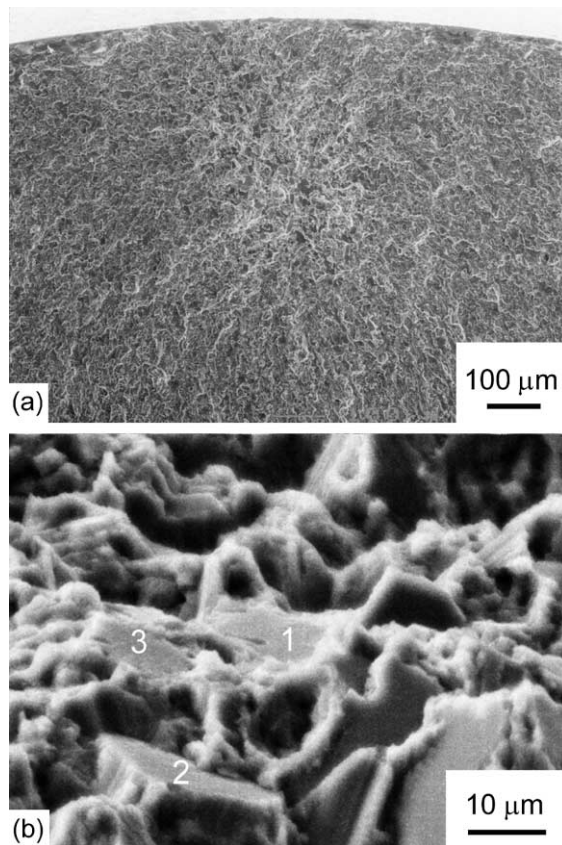
Fig. 7. Fracture surfaces of an *S–N* sample tested at a high load ratio of $R = 0.7$, $\sigma_{max} = 725$ MPa ($N_f = 9.8 \times 10^7$ cycles), showing (a) subsurface crack initiation site (350 μm below surface) and (b) crack initiation and early growth along planar slip bands leading to facet-type fracture surface (specimen tilt: 70°). EBSD analysis of fractured α grains (numbered 1–3) revealed a near-basal orientation of fracture plane.

In addition to the formation of FOD-induced microcracks, the distribution of tensile residual stresses in the K_B specimens was also of importance for crack initiation. X-ray diffraction [13] revealed tensile residual stresses on the side surface of the rectangular gauge section. These tensile stresses, which are formed on the side faces of the tensile specimen due to the proximity of the side surface to the impact crater, proved to be important in the case of low stress, high-cycle behavior in the 10^7–10^8 cycles regime. Confirmed by numerical analysis [12,13], these tensile stresses counterbalance the compressive residual stress field directly beneath the indentation. The numerically estimated distribution of these FOD-induced stresses in the K_B specimen are shown in Fig. 12(a) and (b) for 300 m/s normal impacts (90°) using 1 and 3.2 mm steel shot, respectively. The residual stress fields are calculated with the finite element method using the ABAQUS/ Explicit code, which is based on the explicit time integration method [12]. The dynamic effects, such as inertia, strain rate sensitivity, and stress wave interactions, are included in the simulation. To make connection with experiments, the exact K_B geometries are used, with a clamped–clamped boundary condition prescribed. The substrate is assumed to be elastic-perfectly plastic with a Von Mises surface to specify yield. The yield stress does not vary with strain, but is a function of the strain rate [30]. The rigid contact surface option is used to simulate the rigid projectile, and the option for finite deformation and strain is employed. Full details are given in Refs. [12,13,30].
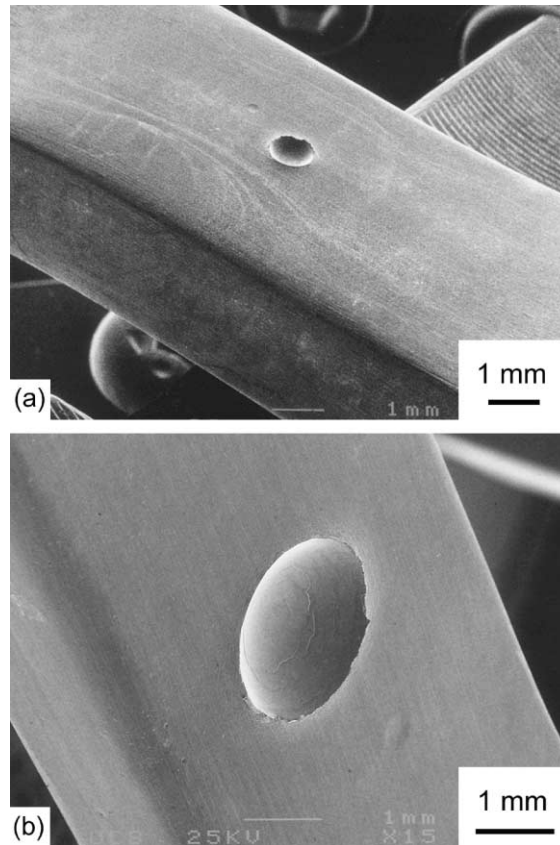
Fig. 8. Gauge section of modified K_B specimens for simulated FOD studies after high-velocity impacts using (a) 1 mm diameter steel sphere and (b) 3.2 mm diameter steel sphere (normal impact angle).

The residual stress distributions for normal impacts display an axis-symmetric stress field with tensile residual stresses (in longitudinal direction) as high as ~220 MPa ($\sigma_{33}/\sigma_y = 0.24$) to 385 MPa ($\sigma_{33}/\sigma_y = 0.42$), where σ_y is the yield stress, and σ_{33} the residual stress in longitudinal direction. The magnitude of these tensile stresses was verified by X-ray diffraction. The corresponding residual stress distribution for an inclined (60°) impact is illustrated in Fig. 12(c) for the case of a 200 m/s, 3.2 mm projectile and shows a highly asymmetric stress field, although the peak residual stresses are similar to those of normal impacts. In particular, the residual stress field on the exit side of the K_B specimen is of same magnitude as the normal impact at the same impact velocity, whereas residual stress field on the entry side corresponds to that of lower speed normal impacts [30]. Furthermore, the residual stresses at the base of the indents are also of similar magnitude for both 90° and 60° impacts [30]. Such residual stresses can have a significant effect on the initiation sites of fatigue cracks and on the value of the fatigue-crack growth thresholds, as discussed below.

3.3. FOD-affected fatigue properties

Stress-life (S–N) data in Fig. 13 clearly show the detrimental effect of FOD on fatigue strength. The reduced lifetimes following impact damage were seen for both projectile sizes, at both low and moderate
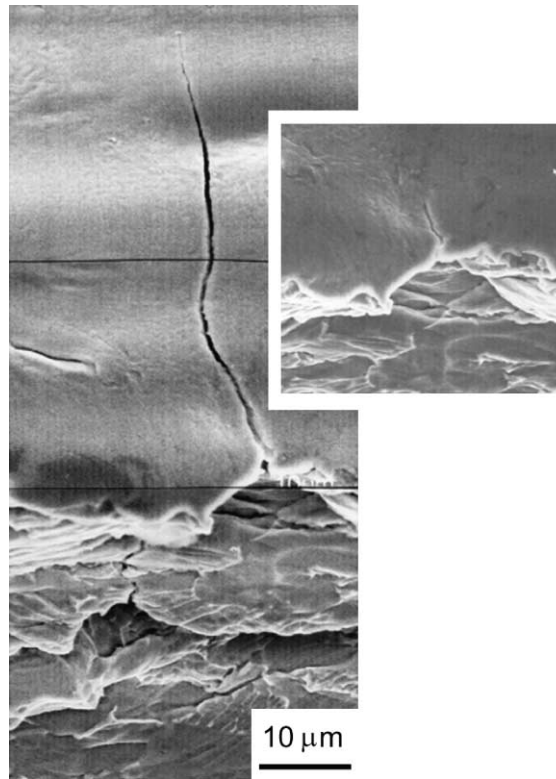
Fig. 9. SEM micrograph of a fatigue crack that formed at a FOD-induced microcrack (small insert). 3.2 mm steel shot, 300 m/s impact velocity. Nominally applied $\sigma_{max} = 500$ MPa, $R = 0.1$, $N = 29,000$ cycles.

load ratios ($R = 0.1$ and 0.5), and both impact angles (although only normal impact data are displayed). As discussed previously [8–10], this detrimental effect of FOD can be considered in terms of premature fatigue-crack initiation resulting from four major factors: (i) the stress concentration of the indent, (ii) FOD-induced microcracking, (iii) plastically deformed microstructure and (iv) residual stresses associated with the impact damage.

Two distinct groups of failures can be identified in Fig. 13, depending upon the magnitude of the applied stresses relative to the tensile residual stresses. At high-applied stresses, HCF failures initiate directly at the impact crater, either at the rim or the base of the crater. Under these conditions, the initiation of a growing fatigue crack is observed at the crater rim at 300 m/s due to the presence of microcracks; conversely, such initiation is observed at the base of the indent at 200 m/s due to the high local stress concentration and the absence of microcracks elsewhere. In contrast, at low-applied stresses (and lower impact velocities), where FOD-induced microcracks were not formed or were much smaller, fatigue cracks were found to initiate away from the indent crater, in regions of substantial tensile residual stresses.

An example of fatigue-crack initiation at low-applied cyclic stresses ($\sigma_{max} = 325$ MPa, $R = 0.1$) in regions away from the damage site in the interior of the specimen is shown in Fig. 14(a) and (b) for 300 m/s impacts by 1 and 3.2 mm diameter shot, respectively. A further example (at $\sigma_{max} = 300$ MPa, $R = 0.1$), where initiation occurred close to surface at the side face of the specimen, is shown in Fig. 14(c). Similarly, fatigue-crack initiation remote from the damage site was observed to occur in the interior of a 60° inclined impacted specimen, as shown in Fig. 14(d) ($\sigma_{max} = 325$ MPa, $R = 0.1$). In all cases, fatigue cracking ini-
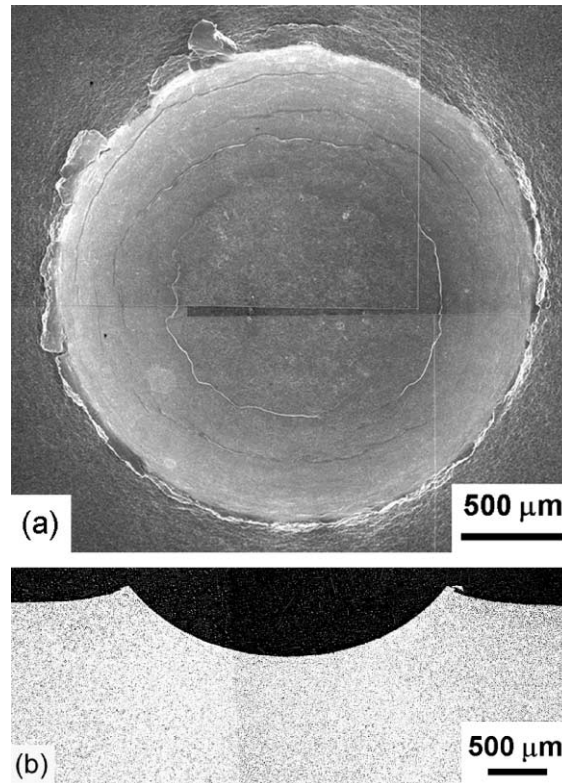
Fig. 10. (a) Scanning electron micrograph and (b) cross-section of impact site after 300 m/s normal (90°) impact using 3.2 mm steel shot.

tiated in regions of the high tensile residual stresses away from the indent; specifically, these residual stresses were on the order of 300 MPa, based on synchrotron X-ray diffraction measurements [13] and numerical computations [12,13] (Fig. 12).

As noted previously, such tensile residual stresses act to elevate the local mean stress (or load ratio), when simply superimposed on the applied far-field fatigue stresses. Based on FOD-related failures at applied cyclic stresses of $\Delta\sigma = 270$–300 MPa at $R = 0.1$ and 250 MPa at $R = 0.5$, superimposing a tensile residual stress of ~300 MPa increases these R-ratios from 0.1 to ~0.5 and from 0.5 to ~0.7, assuming no relaxation (Table 4). The corresponding increase in the maximum stress by this superposition is marked by arrows in the S–N diagram shown in Fig. 13. From these S–N results, it is clear that simple superposition of initial tensile residual stress onto applied far-field stresses provides a significant contribution to the reduction in fatigue life due to FOD.

3.4. FOD-affected fatigue thresholds and fatigue-crack propagation

Thresholds for fatigue-crack growth and the subsequent near-threshold fatigue-crack growth rates of all impacted samples are compared to results for naturally initiated small cracks (~45–1000 μm) [15] and through-thickness large (>5 mm) [11,31] cracks in undamaged material in Fig. 15(a) (for R-ratios of 0.1 and 0.5), in Fig. 15(b) (for projectile sizes of 1 and 3.2 mm), and in Fig. 15(c) (for impact angles of 90° and 60°). The FOD-initiated crack-growth rate data are shown as a function of surface crack length, $2c$, and the
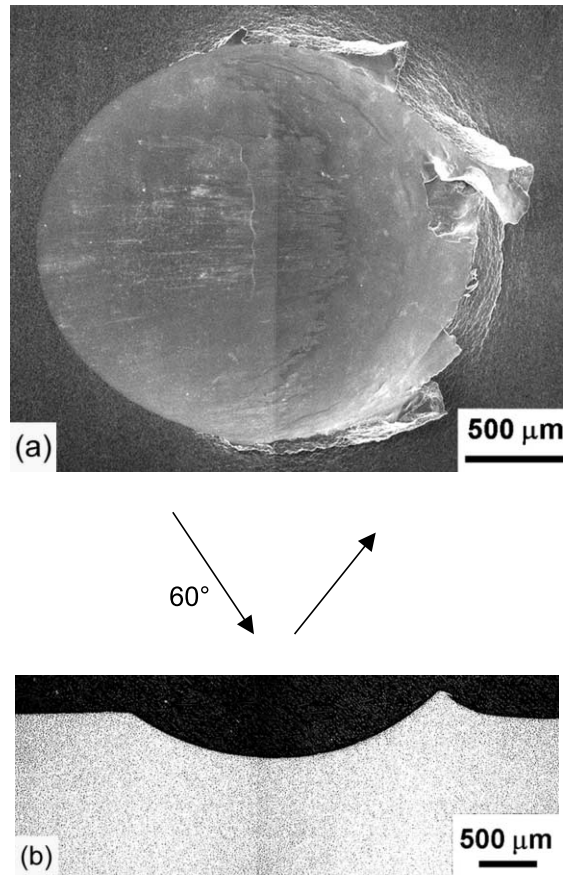
Fig. 11. (a) Scanning electron micrograph and (b) cross-section of impact site after 300 m/s inclined (60°) impact using 3.2 mm steel shot.

approximate applied stress-intensity range (corrected for the stress concentration of the indent using Eq. (1)). Crack-growth rate data of the FOD-induced microcracks ($2c \sim 5$–100 μm), which are truly micro-structurally small cracks, fall into a single scatter band for all impact conditions under study (Fig. 15(a)–(c)). Specifically, comparable growth-rate data of microcracks at low ($R = 0.1$) and moderate ($R = 0.5$) load ratios indicate that mean stresses play little role in small-crack propagation (Fig. 15(a)). In general, the growth rates of the FOD-initiated small cracks were at least an order-of-magnitude faster than the cor-responding large-crack results at near-threshold levels. Such an effect is typical for cracks with dimensions comparable to microstructural size-scales [e.g., 32–35]. However, the large and small-crack results tend to merge above a ΔK of ~ 10 MPa $\sqrt{m}$, as the small cracks grow to dimensions substantially larger than the microstructure, consistent with the development of crack closure associated with the progressively in-creasing wake of the small cracks. In addition, at these higher ΔK levels, the progressively increasing length of the crack front experiences a statistical sampling of a representative average of all microstructural barriers, similar to the large cracks.

An additional factor associated with the faster growth rates of the FOD-initiated microcracks is the microstructural changes associated with impact-induced plasticity. This is evident from shot-peening ex-periments on Ti–6Al–4V where, by separating the effect of deformation from residual stresses, it has been
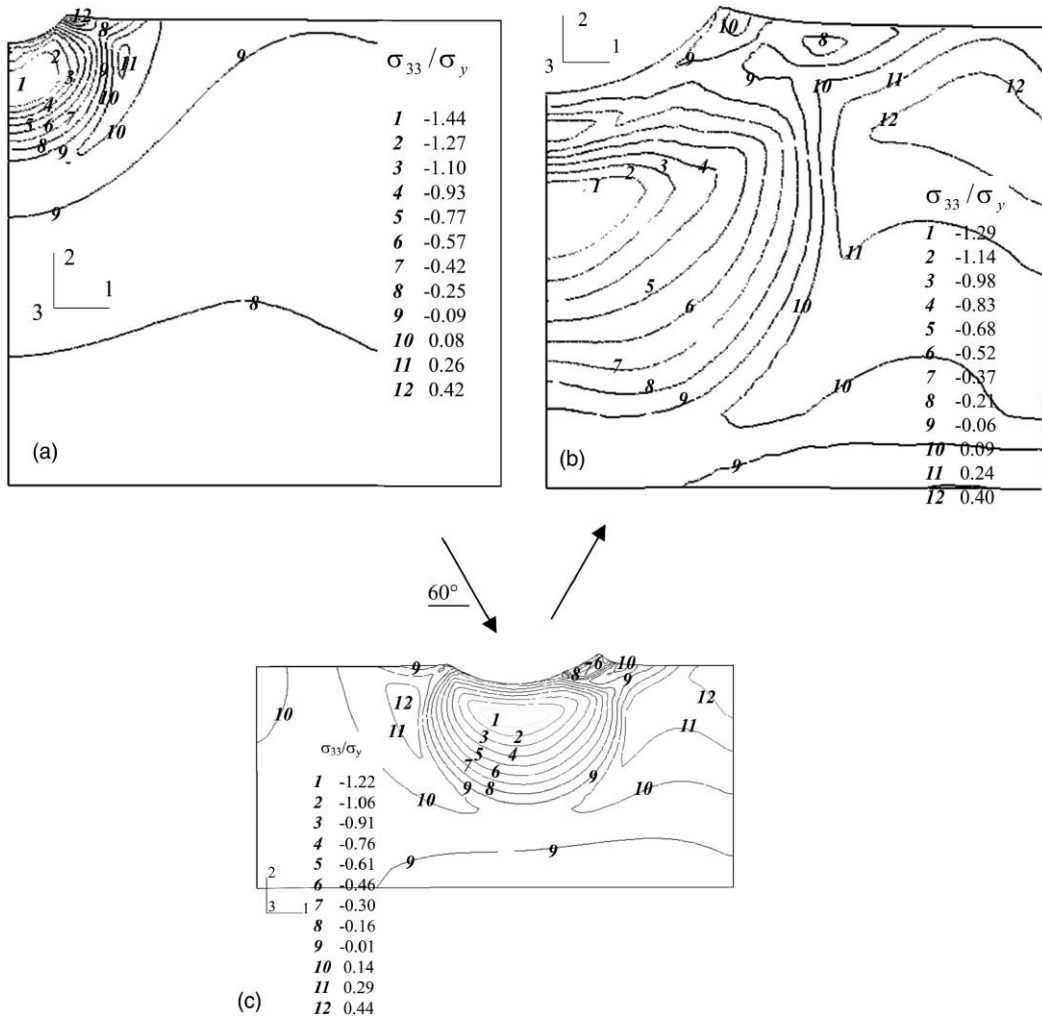
Fig. 12. Residual stress distribution in plane perpendicular to longitudinal axis of K_B specimen, after 300 m/s normal (90°) impact using (a) 1 mm and (b) 3.2 mm diameter steel shot, or (c) 200 m/s inclined (60°) impact using 3.2 mm steel shot. After Chen and Hutchinson [12]. σ_{ii} = normal residual stress, σ_y = yield stress (915 MPa).

observed that the deformed microstructure, with its inherently high dislocation density, showed a reduced resistance to crack growth [26,27].

As discussed elsewhere [11,31], the large-crack thresholds shown in Fig. 15 were determined up to the highest load ratios ($R \sim 0.91$–0.95) under constant-K_{max}/increasing-K_{min} loading conditions chosen to minimize the effect of crack closure. Accordingly, for the bimodal Ti–6Al–4V microstructure, the measured threshold of $\sim$1.9 MPa $\sqrt{m}$ at $R = 0.95$ is considered to be a worst-case threshold for cracks of dimensions large compared to the scale of the microstructure. However, observations show that the smallest FOD-initiated cracks, which have dimensions comparable with microstructural size-scales ($\sim$2–10 μm), can propagate at stress intensities well below these worst-case thresholds, specifically at applied stress intensities as low as $\Delta K \sim 1$ MPa $\sqrt{m}$, presumably due to biased sampling of the "weak links" in the microstructure. Based on the results shown in Fig. 15, it is clear that a concept of a worst-case threshold (determined under
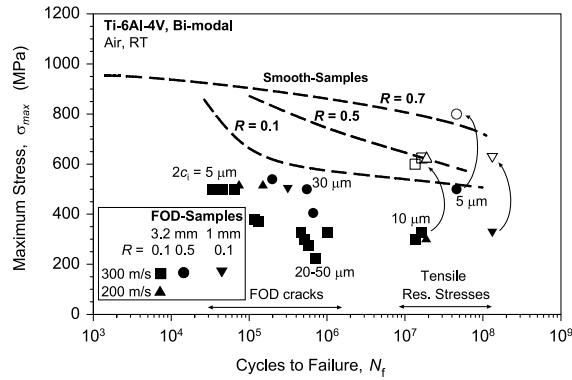
Fig. 13. S–N data showing reduced fatigue life due to simulated FOD (normal impact) as compared to smooth-bar specimens in bimodal Ti–6Al–4V. $2c_i$ is the surface crack length of FOD-induced microcracks. For failures at 10^7–10^8 cycles, the effect of local tensile residual stress ($\sim$300 MPa) in increasing the local maximum stress (and hence the local load ratio) is illustrated by arrows and open symbols.
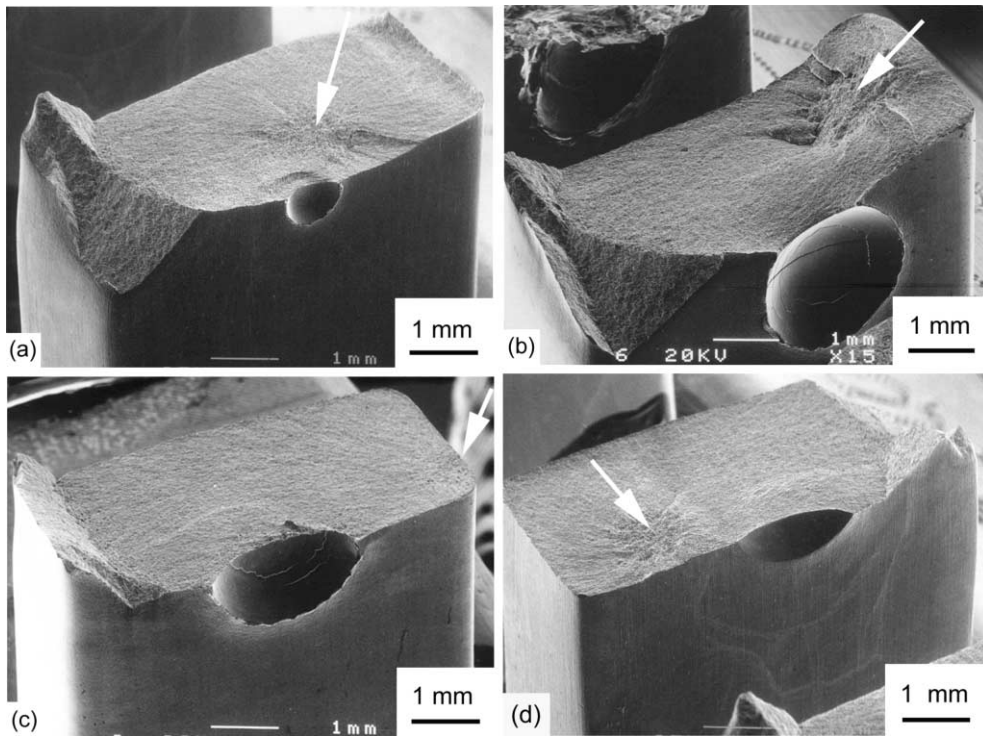

Fig. 14. Lower stress fatigue loading after 300 m/s impact (90°) using 1 or 3.2 mm diameter steel shot caused crack initiation away from the indent site (marked by arrows): (a) 1 mm steel shot, nominally applied $\sigma_{max} = 325$ MPa, $R = 0.1$, $N_f = 1.3 \times 10^8$ cycles, (b) 3.2 mm steel shot (90°), nominally applied $\sigma_{max} = 325$ MPa, $R = 0.1$, $N_f = 1.6 \times 10^7$ cycles, and (c) nominally applied $\sigma_{max} = 300$ MPa, $R = 0.1$, $N_f = 1.3 \times 10^7$ cycles. (d) 200 m/s inclined impact (60°) using 3.2 mm steel shot, nominally applied $\sigma_{max} = 325$ MPa, $R = 0.1$, $N_f = 1.5 \times 10^8$ cycles.

$R \rightarrow 1$ conditions that minimize crack closure) applies strictly for homogeneous continuum-sized cracks larger than microstructural size-scales. This concept does not provide a lower-bound threshold stress in-

Table 4
Superposition of initial tensile residual stress on nominally applied cyclic stress

Load ratio, R ($\sigma_{min}/\sigma_{max}$)	σ_{min}	σ_{max}	σ_{res}	$\sigma_{min,eff}$ ($\sigma_{min} + \sigma_{res}$)	$\sigma_{max,eff}$ ($\sigma_{max} + \sigma_{res}$)	Effective load ratio, R_{eff} ($\sigma_{min,eff}/\sigma_{max,eff}$)
0.1	30	300	300	330	600	0.55
0.1	33	325	300	333	633	0.53
0.5	250	500	300	550	850	0.69

σ_{min}: applied minimum stress, σ_{max}: applied maximum stress, σ_{res}: residual stress, $\sigma_{min,eff}$: effective minimum stress, $\sigma_{max,eff}$: effective maximum stress. All stresses are in MPa.

tensity for cracks on the scale of microstructural dimensions, as can be the case in the earliest stages of FOD-induced fatigue failure.

The full *quantitative* effect of the FOD-induced residual stresses on fatigue failures at 10^5–10^6 cycles where fatigue cracks initiated directly at the impact site is still under study. Although simple superposition of the residual and applied stresses was considered above for low-applied stresses ($\sigma_{max} = 325$ MPa, $R = 0.1$), recent numerical modelling and in situ synchrotron X-ray diffraction results have indicated that at high-applied stresses ($\sigma_{max} = 500$ MPa, $R = 0.1$) during the first few fatigue cycles, significant relaxation of both the tensile and compressive residual stresses (by typically ~30%), can occur [13].

What is interesting here is that due to plastic deformation (aided by the Bauschinger effect) at the FOD indentation site when the high stresses (relative to the level of residual stresses) are applied, the compressive stresses at the base of the crater are partially relaxed, permitting crack initiation to occur there for low impact velocities due to the higher stress concentration [8,9]. The tensile residual stresses at the crater rim are also relaxed, but due to the presence of microcracks following 300 m/s impacts this still is the preferred site for crack initiation at higher impact velocities. Thus, for subsequent fatigue cycling at high-applied stresses, the FOD-induced residual stresses do not play a major role on the initial crack growth of FOD-induced microcracks ($2c \sim 5$–100 μm) due to their relaxation on cyclic loading.

There are conditions, however, where relaxation does not occur or substantial residual stresses are stable during cycling. Most specifically, the rate and extent of relaxation is a function of the applied stresses. When the applied stresses are low enough, the residual stresses are stable and relaxation is not observed. Therefore, the regions closest to the indent exhibit the greatest degree of relaxation, due to the stress concentrating effects of the indent on the applied stresses. It is thought that this explains the stability (and hence importance) of the tensile residual stresses far from the indent even under conditions where the residual stresses near the indent show substantial relaxation.

Moreover, the stress field ahead of a propagating crack can potentially serve to further relax the residual stresses. This crack-driven relaxation becomes increasingly important as the crack grows to larger crack sizes under a fixed load amplitude, due to the increase in the ΔK field ahead of the tip. This may explain the factor-of-six longer life exhibited by an indent formed by a 1 mm projectile compared to a 3.2 mm projectile (both formed at 300 m/s). In spite of the similar features (pile-up, microcracking, shear bands), and similar aspect ratio of the craters, the absolute proximity of the retarding compressive zone beneath the crater base is different. As illustrated in Fig. 16, the rim-crack formed in the smaller indent is still quite small ($2c \sim 0.7$ mm) by the time it reaches any mitigating residual compressive stresses beneath the base, whereas the rim-crack formed in the large indent has grown to a substantial size ($2c \sim 2.5$ mm) by the time it has reached the compressive zone beneath the base. It is thought that the larger crack size results in more substantial relaxation of any mitigating compressive residual stresses, thereby leading to a shorter propagation time. Moreover, larger impact indentation sites also lower the overall fatigue life due to initial crack size effects. Once a growing fatigue crack initiates, the effective initial crack size is larger in the case with larger indentation site, and hence it propagates initially faster.
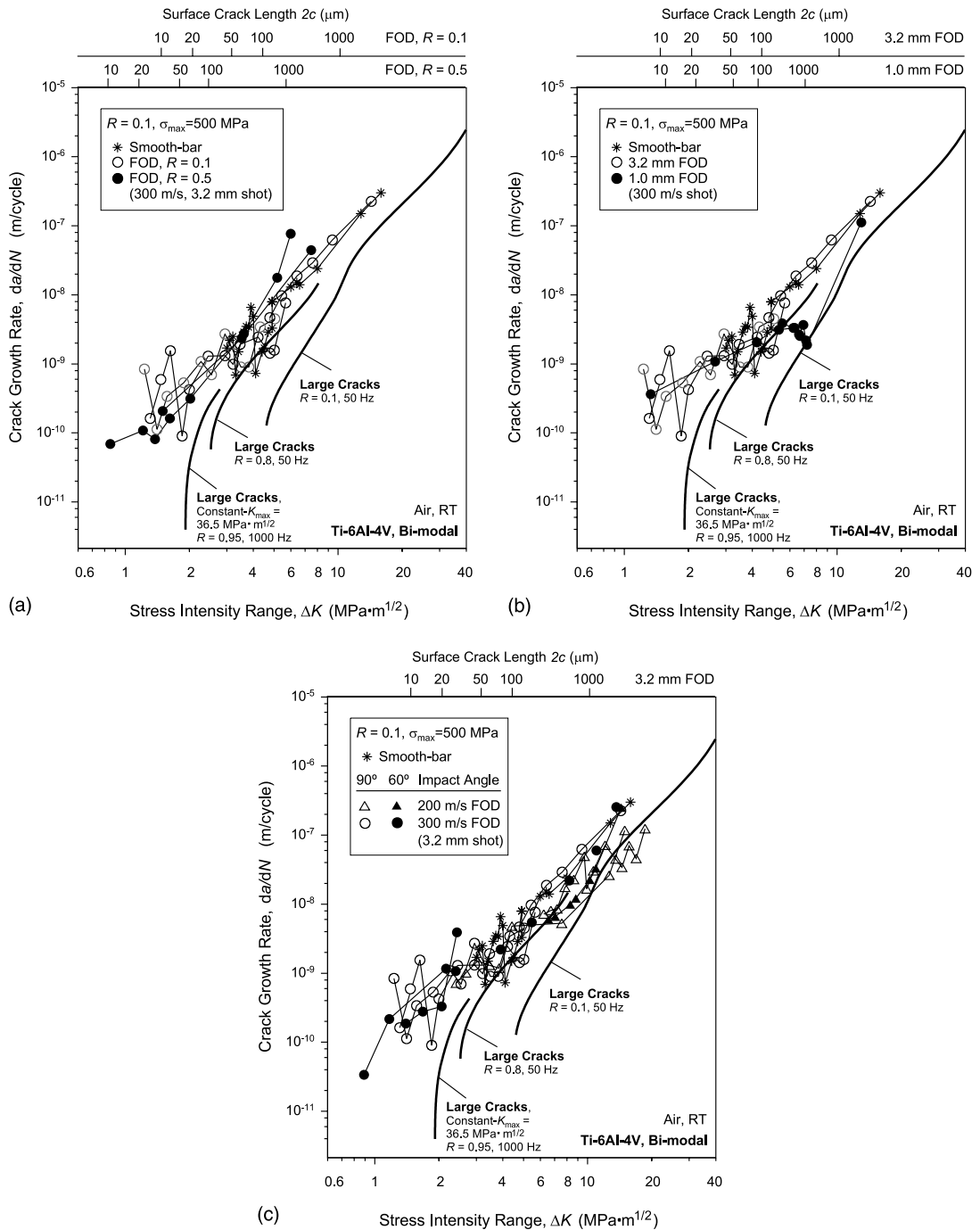
Fig. 15. Fatigue crack-growth rate data of FOD-induced small cracks emanating directly from FOD impacts as a function of (a) load ratio ($R = 0.1$ and 0.5), (b) projectile size (1 and 3.2 mm), and (c) impact angle (60° and 90°). FOD-initiated small-crack growth-rate data are compared to (smooth-bar) naturally initiated small-crack [15] and through-thickness large-crack results in undamaged bi-modal Ti–6Al–4V. Large-crack growth rates for $R = 0.1$ and 0.8 were derived from constant load-ratio tests, whereas for $R = 0.95$ constant-K_{max}/increasing-K_{min} testing was used [11,31].
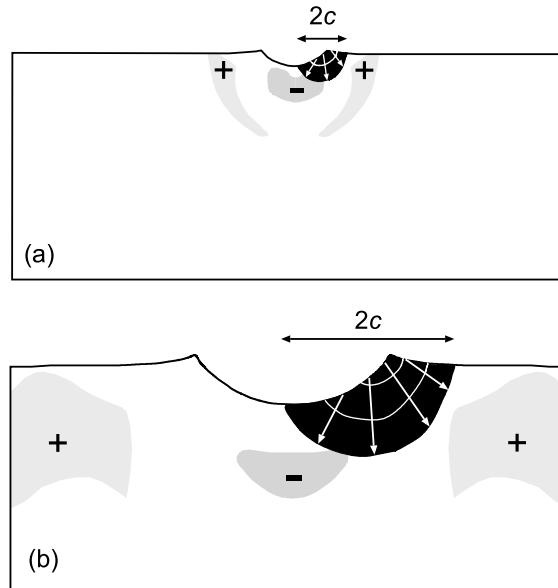
Fig. 16. Schematic display of progressive positions of crack fronts and relative sizes of cracks at the point when the cracks encounter the prominent compressive residual stress region beneath indentation site of (a) 1 mm and (b) 3.2 mm steel shot impacts.

3.5. Threshold conditions based on the Kitagawa–Takahashi diagram

Previous work [9,10] has illustrated the utility of the Kitigawa–Takahashi diagram [36] in evaluating the limiting conditions for FOD-induced HCF failures when the applied stress ranges are high (relative to the magnitude of the residual stress) and cracks are formed directly at the impact site. Here, the limiting threshold conditions were defined by the stress-concentration corrected smooth-bar fatigue limit (at microstructurally small crack sizes) and a ''worst-case'' fatigue-crack growth threshold (at larger ''homogeneous continuum-sized'' crack sizes). A more favorable representation of the failure envelopes for the two load ratios of 0.1 and 0.5 in Fig. 17 can be made using the El Haddad et al. [37] empirical quantification of Kitagawa–Takahashi approach; this approach introduces a constant, termed the intrinsic crack length, $2c_0$, such that the stress intensity is defined as $\Delta K = Y\Delta\sigma\sqrt{\pi(2c + 2c_0)}$, where Y is the geometry factor.

It is now possible to extend the application of the Kitagawa–Takahashi diagram to include cracks formed far from the indent by evaluating the effective R-ratio induced by the superposition of stable residual stresses. Using the fatigue failures plotted in Fig. 17 as data points at surface crack lengths of $2c = 1$ μm, and superimposing the measured tensile residual stress of $\sim$300 MPa, the R-ratios are increased from 0.1 to $\sim$0.5 and from 0.5 to $\sim$0.7 at far-field stress range of $\sim$300 MPa (Table 4). Accordingly, such failures at both load ratios can still be described by the proposed Kitagawa–Takahashi approach, provided the limiting conditions are given by the stress concentration *and* residual stress corrected smooth-bar fatigue limit at small crack sizes and the ''worst-case'' threshold for larger crack sizes.

4. Conclusions

Based on a study of the role of FOD in affecting HCF failures in a turbine engine Ti–6Al–4V alloy with a bimodal (STOA) microstructure, the following conclusions can be made:
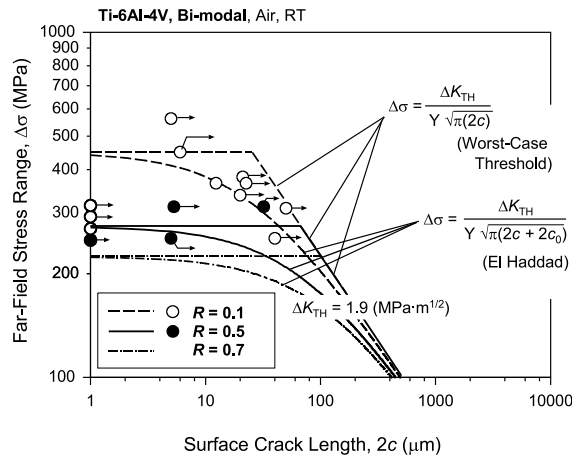
Fig. 17. Modified Kitagawa–Takahashi diagram representing the limiting threshold crack-growth conditions ($da/dN = 10^{-11}$–10^{-10} m/cycle) at $R = 0.1$ and 0.5 for FOD-induced small cracks in bimodal Ti–6Al–4V. Plotted is the threshold stress range as a function of surface crack length. The limiting conditions are defined by the worst-case ΔK_{TH} threshold for "homogeneous continuum-sized" cracks (at large crack sizes) and the smooth-bar fatigue limit, corrected for stress concentration and residual stresses (at smaller crack sizes). Accordingly, data points are corrected for the stress concentration of the FOD indents.

1. FOD, simulated by the high-velocity (200–300 m/s) impact of steel spheres (1 and 3.2 mm diameter) at impact angles of 60° and 90° on a flat specimen surface, markedly reduced the fatigue performance. The principal effect of FOD was to induce preferred sites for the premature initiation of fatigue cracks.
2. Premature crack initiation was caused by the interplay of a number of factors, specifically (i) the stress concentration due to the FOD indentation, (ii) the creation (at highest impact velocities only) of micro-cracks at the crater rim of the damaged zone, (iii) microstructural damage from FOD-induced plastic deformation, and (iv) the localized presence of tensile residual stresses around the indent.
3. Since such microcracking at the crater rim (and indeed the shear band formation) could only be de-tected at the sites of the higher velocity impacts, it is concluded that low-velocity or quasi-static inden-tations cannot provide a worst-case simulation of FOD.
4. The magnitudes of the residual stresses in the vicinity of the damage sites have been computed numer-ically and measured experimentally using synchrotron X-ray diffraction. Prior to fatigue cycling, peak tensile values of these residual stresses are on the order of 300 MPa and are located in the interior ad-jacent to the highly deformed region beneath the indentations.
5. Two groups of FOD-induced HCF failures could be identified. The first group involved the initiation of growing fatigue cracks directly at the impact site and caused failures within 10^5–10^6 cycles. At *stress-con-centration corrected* stress ranges from 250 to 560 MPa, FOD-initiated microcracks ($\sim$2–10 μm in size) propagated from both 60° and 90° impact sites at applied stress intensities below a ΔK of 1 MPa $\sqrt{m}$ (at both $R = 0.1$ and 0.5) and showed no pronounced threshold behavior, i.e., small-crack growth occurred at driving forces well below the "worst-case" ΔK_{TH} threshold of 1.9 MPa $\sqrt{m}$ for cracks larger than the characteristic microstructural size-scales in this alloy. The proposed criterion for such failures has been described by a modified Kitagawa–Takahashi approach, where the limiting threshold conditions are de-fined by the stress-concentration corrected smooth-bar fatigue limit (at microstructurally small crack sizes) and the "worst-case" ΔK_{TH} threshold (at larger "homogeneous continuum-sized" crack sizes).
6. The second group of failures at 10^7–10^8 cycles initiated at locations remote from impact damage in re-gions of high tensile residual stresses. It was found that simple superposition of the initial tensile resid-ual stresses onto the applied stresses provided a significant contribution to the reduction in fatigue

strength by affecting the local mean stress and load ratio. Accordingly, the modified Kitagawa–Takahashi approach proposed above must be additionally corrected for the presence of tensile residual stresses to account for such failures. With this correction, this approach provides a rational basis for the effect of FOD on HCF failures in Ti–6Al–4V.

Acknowledgements

References

[1] Cowles BA. High cycle fatigue in aircraft gas turbines—an industry perspective. Int J Fract 1996;80:147–63.
[2] Nicholas T, Zuiker JR. On the use of the Goodman diagram for high cycle fatigue design. Int J Fract 1996;80:219–35.
[3] Larsen JR, Worth BD, Annis Jr CG, Haake FK. An assessment of the role of near-threshold crack growth in high cycle fatigue life prediction of aerospace titanium alloys under turbine engine spectra. Int J Fract 1996;80:237–55.
[4] Nicholas T. Critical issues in high cycle fatigue. Int J Fatigue 1999;21:S221–31.
[5] Nicholas T, Barber JR, Bertke RS. Impact damage on titanium leading edges from small hard objects. Exp Mech 1980;October:357–64.
[6] Hudak SJ, Chan KS, McClung RC, Chell GG, Lee Y-D, Davidson DL. High Cycle Fatigue of Turbine Blade Materials, Final technical report UDRI subcontract no. RI 40098X SwRI project no. 18-8653, 1999.
[7] Ritchie RO. Small cracks and high-cycle fatigue. In: Chang JCI, Coulter J, Brei D, Martinez WHG, Friedmann PP, editors. Proceedings of the ASME Aerospace Division, AD-vol. 52. Warrendale, PA: ASME; 1996. p. 321–33.
[8] Peters JO, Roder O, Boyce BL, Thompson AW, Ritchie RO. Role of foreign-object damage on thresholds for high-cycle fatigue in Ti–6Al–4V. Metall Mater Trans A 2000;31A:1571–83.
[9] Peters JO, Ritchie RO. Influence of foreign-object damage on crack initiation and early crack growth during high-cycle fatigue of Ti–6Al–4V. Eng Fract Mech 2000;67:193–207.
[10] Peters JO, Ritchie RO. Foreign-object damage and high-cycle fatigue: role of microstructure in Ti–6Al–4V. Int J Fatigue 2001;23:S413–21.
[11] Ritchie RO, Davidson DL, Boyce BL, Campbell JP, Roder O. High-cycle fatigue of Ti–6Al–4V. Fatigue Fract Eng Mater Struct 1999;22:621–31.
[12] Chen X, Hutchinson JW. Foreign object damage and fatigue crack threshold: cracking outside shallow indents. Int J Fract 2001;107:31–51.
[13] Boyce BL, Chen X, Hutchinson JW, Ritchie RO. The residual stress state due to a spherical hard-body impact. Mech Mater 2001;33:441–54.
[14] Eylon D. Summary of the Available Information on the Processing of the Ti–6Al–4V HCF/LCF Program Plates, University of Dayton Report, Dayton, OH, 1998.
[15] Hines JA, Peters JO, Lütjering G. Microcrack propagation in Ti–6Al–4V alloys. In: Boyer RR, Eylon D, Lütjering G, editors. Fatigue behavior of titanium alloys. Warrendale, PA: TMS; 1999. p. 15–22.
[16] Morgan JM, Milligan WW. A 1 kHz servohydraulic fatigue testing system. In: Soboyejo WO, Srivatsan TS, editors. High cycle fatigue of structural materials. Warrendale, PA: TMS; 1997. p. 305–12.
[17] Lukáš P. Stress intensity factor for small notch-emanating cracks. Eng Fract Mech 1987;26:471–3.
[18] Newman Jr JC, Raju IS. An empirical stress-intensity factor equation for the surface crack. Eng Fract Mech 1981;15:185–92.
[19] Nisida M, Kim P. Stress concentration caused by the presence of a spherical cavity or a spherical-surfaced hollow. In: Proceedings of the Twelfth National Congress on Applied Mechanics, 1962. p. 69–74.
[20] Ravichandran KS, Li X-D. Fracture mechanical character of small cracks in polycrystalline materials: concept and numerical K calculations. Acta Mater 2000;48:525–40.

[21] Ravichandran KS. Three-dimensional crack-shape effects during the growth of small surface fatigue cracks in a titanium-base alloy. Fatigue Fract Eng Mater Struct 1997;20:1423–42.

[22] Bellows RS, Muju S, Nicholas T. Validation of the step test method for generating Haigh diagrams for Ti–6Al–4V. Int J Fatigue 1999;21:687–97.

[23] Morrisey RJ, McDowell DL, Nicholas T. Frequency and stress ratio effects in high cycle fatigue of Ti–6Al–4V. Int J Fatigue 1999;21:679–85.

[24] Murakami Y, Nomoto T, Ueda T. Factors influencing the mechanism of superlong fatigue failure in steels. Fatigue Fract Eng Mater Struct 1999;22:581–90.

[25] Murakami Y, Takada M, Toriyama T. Super-long life tension-compression fatigue properties of quenched and tempered 0.46% carbon steel. Int J Fatigue 1998;16:661–7.

[26] Wagner L, Lütjering G. Influence of shot peening parameters on the surface layer properties and the fatigue life of Ti–6Al–4V. In: Fuchs HO, editor. Proceedings of the 2nd International Conference on Shot Peening. Paramus, NJ: American Shot Peening Society; 1984. p. 194–200.

[27] Wagner L, Lütjering G. Influence of a shot peening treatment on the fatigue limit of Ti–6Al–4V. In: Fuchs HO, editor. Proceedings of the 2nd International Conference on Shot Peening. Paramus, NJ: American Shot Peening Society; 1984. p. 201–7.

[28] Adachi S, Wagner L, Lütjering G. Influence of microstructure and mean stress on fatigue strength of Ti–6Al–4V. In: Lütjering G, Zwicker V, Bunk W, editors. Titanium science and technology Proceedings of the 5th International Conference on Titanium. Oberursel, Germany: DGM; 1985. p. 21–39.

[29] Evans WJ, Bache MR. Dwell-sensitive fatigue under biaxial loads in the near-alpha titanium alloy IMI685. Int J Fatigue 1994;16:443–52.

[30] Chen X. Foreign-object damage and fatigue cracking. PhD thesis. Harvard University, Cambridge, 2001.

[31] Boyce BL, Ritchie RO. Effect of load ratio and maximum stress intensity on the fatigue threshold in Ti–6Al–4V. Eng Fract Mech 2001;68:129–47.

[32] Ritchie RO, Peters JO. Small fatigue cracks: mechanics, mechanisms and engineering applications. Mater Trans 2001;42:58–67.

[33] Suresh S, Ritchie RO. Propagation of short fatigue cracks. Int Metals Rev 1984;29:445–76.

[34] Miller KJ, de los Rios ER, editors. The behaviour of short fatigue cracks. London, UK: Mechanical Engineering Publication; 1986.

[35] Ritchie RO, Lankford J, editors. Small fatigue cracks. Warrendale, PA: TMS–AIME; 1986.

[36] Kitagawa H, Takahashi S. Applicability of fracture mechanics to very small cracks or the cracks in the early stage. In: Proceedings of the Second International Conference on Mechanical Behavior of Materials. Metals Park, OH: ASM; 1976. p. 627–31.

[37] El Haddad MH, Topper TH, Smith KN. Prediction of non propagating cracks. Eng Fract Mech 1979;11:573–84.